Effect of ultrasonic melt processing and Al-Ti-B on the microstructural refinement of recycled Al alloys

Yuliang Zhao [a,b,*], Weixiang He [a], Dongfu Song [c,d,*], Fanghua Shen [a], Xinxin Li [a], Zhenzhong Sun [a], Yao Wang [e], Shuhong Liu [f], Yong Du [f], Ricardo Fernández [b,*]

[a] Neutron Scattering Technical Engineering Research Centre, School of Mechanical Engineering, Dongguan University of Technology, Dongguan 523808, China
[b] Centro Nacional de Investigaciones Metalúrgicas (CENIM), C.S.I.C., Avda. de Gregorio del Amo 8, Madrid 28040, Spain
[c] National Engineering Research Centre of Near-net-shape Forming for Metallic Materials, South China University of Technology, Guangzhou 510641, China
[d] Guangdong Provincial Key Laboratory of Metal Toughening Technology and Application, Institute of New Materials, Guangdong Academy of Sciences, Guangzhou 510650, China
[e] Centre of Excellence for Advanced Materials, Dongguan, Guangdong 523808, China
[f] State Key Laboratory of Powder Metallurgy, Central South University, Changsha 410083, China

ARTICLE INFO

ABSTRACT

Refining the α-Al grain size and controlling the morphology of intermetallic phases during solidification of Al alloys using ultrasonic melt processing (USMP) and Al-Ti-B have been extensively used in academic and industry. While, their synergy effect on the formation of these phases has not yet clearly demonstrated. In this paper, the influence of USMP and Al-Ti-B on the solidified microstructure of multicomponent Al-4.5Cu-0.5Mn-0.5Mg-0.2Si-xFe alloys (x = 0.7, and 1.2 wt%) has been comparatively studied. The results show that the USMP + Al-Ti-B method produce a more profound refinement effect than the individual methods. In addition, the area of single Fe-rich phases in both alloys with USMP + Al-Ti-B are also refined compared with conventional methods. A mechanism is proposed for the refinement, which are the deagglomerated TiB$_2$ parties induced by USMP providing more effective nucleation sites for α-Al, and the refined interdendritic regions limited the growth of Fe-rich phases in the following eutectic reaction. Finally, the application of combined USMP + Al-Ti-B methods is feasible in microstructural refinement, resulting in the improving the casting soundness and mechanical properties of alloys.

1. Introduction

Al–Cu alloys have a high strength-to-density ratio, and good fatigue and damage tolerance, which is widely used in aerospace and engineering structure applications [1–3]. Nowadays, a large number of aircrafts have reached the end of their service life. Their number will increase in the coming years, providing an abundant sources of valuable recycled metals, a large part of which are Al-Cu alloys. Thanks to the high recyclability and sustainability of Al, most of these Al scraps are recycled, which leads to reduce energy consumption, reducing greenhouse gas and solid waste, promoting circular economy [4,5].

However, due to the various sources of Al scraps and use of iron-based tools, these impurity elements, such as, Fe and Si, are easily

introduced to the recycled Al alloys [6–9]. Fe is the main impurity element in Al-Cu alloys, that form hard and brittle plate-like Fe-rich intermetallic phases (named Fe-rich phases hereinafter) during solidification [10–29]. The type of Fe-rich phases in Al-Cu alloys, such as, Al$_3$(CuFe), Al$_6$(CuFe), Al$_7$Cu$_2$Fe (β-Fe), Al$_{15}$Fe$_3$(SiCu)$_2$ (α-Fe), varies with different alloy compositions, cooling rates, and external fields during solidification [12–23]. The presence of these brittle particles (especially the large sizes) in the alloys significantly decreases the fatigue strength and ductility of the alloys [10–14]. In order to avoid these problems and foster the use of these recycled Al alloys, various methods are used: 1) The chemical route to change the morphology of Fe-rich particles by adding trace elements or grain refiner before solidification [15–21]; 2) applying ultrasonic or electromagnetic fields to refine the

microstructure during solidification [22–25]; 3) using heat treatments or thermomechanical processing, such as rolling or extrusion, to broke the Fe-rich particles after solidification [26–29]. In some alloys, Fe is deliberately added for improving their strength at room temperature [30,31] or their high-temperature properties [32,33]. Hence, it is necessary to optimize in-service condition of recycled Al alloys by adjusting the Fe content and Fe-rich particles morphology.

It is well accepted that the Al-5Ti-1B master alloy has Al_3Ti and TiB_2 nucleant particles. This plays a critical role in the grain refinement, reducing pores and micro-segregations reduction, which enhances Al alloys mechanical properties [43–48]. Moreover, the Al-5Ti-1B addition can alter the solidification sequence and change the morphology of Fe-rich phases in Al alloys during solidification [34–42]. The influence of Al-5Ti-1B can be ascribed to the following three aspects: 1) refinement of the Fe-rich particles size without changing their type [35–36,42]; 2) promotion of the formation of plate-like Fe-rich phases [37–40]; 3) promotion of the transformation of Fe-rich phases from plate-like to Chinese-script [20,21,41]. The formation of different Fe-rich phases depends on the alloy composition and cooling rate. Al-5Ti-1B addition to Al-Mg alloys [35,36] not only refine the primary Al grains but also refines the α-Fe particles. Both effects are related through the refinement of Al grains that limits the growth of α-Fe phases in the interdendritic liquid regions during subsequently eutectic reaction.

The size of primary Al_3Fe phases in Al-Fe alloys is also reduced by Al-5Ti-1B addition [42]. Submicron-scale tomography results in Al-Mg-Si alloy [37] clearly demonstrated that Al-5Ti-1B reduces the number and length of α-Fe and β-Al$_5$FeSi (β-Fe) particles. This improvement is produced because TiB_2 act as nucleation site for α-Fe and β-Fe. Moreover, some researchers [38–40] found that Al-5Ti-1B induces the formation of β-Fe phases in Al-Si alloys. They deduced that TiB_2 particles have a small misfit with β-Fe phase. In our previous studies [20,21], it has been shown that the addition of Al-5Ti-1B to Al-Fe and Al-Cu-Fe alloys promotes the formation of Al_6Fe phases and inhibit the growth of primary Al_3Fe phases. However, the study of Al-5Ti-1B addition on the solidification sequence and distribution of Fe-rich phases of high-Fe-containing recycled Al-Cu alloys remains unknown.

Ultrasonic melt processing, USMP, is a promising economical technology that provides an environment-friendly method for improving the soundness and quality of cast ingots [43–48]. It is generally believed that the action mechanisms of USMP on solidifying microstructure can be ascribed to two aspects: 1) the cavitation bubbles generated by acoustic cavitation that continually attack and broke the dendritic structure and the intermetallic phases; 2) acoustic streaming improves solute homogeneity which homogenizes the spatial distribution of dendrites and intermetallic phases [43–45]. Extensive works have been conducted to demonstrate that USMP refines the Al grain size, improve the microstructural homogenisation, and enhance the properties of Al alloys [49–55]. Moreover, it has been demonstrated that the USMP reduces the macro-segregation and boosts the formation of fine and homogenously distributed Fe-rich phases in Al-Si-Fe alloys [56,57]. Also, the USMP has been used to tune the Fe-rich phases in Al alloys at different solidification stages [56–63]. Moreover, the USMP changes the shape of α-Fe phases from coarse Chinese-script to fine polygonal type in Al-Si alloys [58]. At melt temperatures below 600 °C, the acoustic streaming distributes the solute homogenously. At melt temperatures of 600–750 °C, the acoustic cavitation promotes the nucleation and breaks the large particles. The morphology of primary Al_3Fe phases in Al-Fe alloys changes from plate-like to blocky and granular shape by applying USMP, which is due to cavitation-induced fragmentation of primary Al_3Fe and enhances the nucleation and refines the size of Al_3Fe. Both effects improve the mechanical properties of the alloys [60]. The size of α-Fe in Al-Si alloys is also greatly reduced by acoustic cavitation during USMP [61]. Acoustic streaming and cavitation of USMP homogenize the solute distribution and the temperature fields in Al-Si alloys. This results in the presence of refined δ-Al$_4$(FeMn)Si$_2$ Fe-rich particles [62]. In Al-Si-Fe alloys the plate-like β-Al$_9$Si$_2$Fe$_2$ phases was

replaced by star-like α-Al$_{12}$Si$_2$Fe phases [63]. This morphological modification and phase transformation is due to the acoustic cavitation that induces melt undercooling and increases the nucleation of Fe-rich phases. However, to author's knowledge, the combined effect of USMP and Al-5Ti-1B on the solidification sequences and growth of Fe-rich phases in recycled Al-Cu alloys have not been reported yet.

Hence, the effect of USMP and Al-Ti-B on the growth of α-Al and Fe-rich phases in Al-Cu-Mn-Mg-Fe-Si alloys is comparatively studied in the present work. Optical microscope (OM), scanning electron microscope (SEM), electron backscatter diffraction (EBSD), differential scanning calorimeter (DSC) and thermal analysis were used to characterize the microstructural evolution of the alloy during solidification. The detailed mechanism of USMP + Al-Ti-B on the growth of α-Al and Fe-rich phases is briefly discussed.

2. Materials and methods

2.1. Alloy preparation

Commercial pure Al (99.8 %), Al-50Cu, Al-20Fe, Al-10Mn, Al-10Mg and Al-20Si master alloys were used to produce the studied alloys. The selection of Al-Cu-Mn-Mg-Si-Fe alloys is based on the A206 alloy, which has high mechanical properties and is widely used in the aerospace and automotive sectors. These alloys were added to a graphite crucible for melting and they were heated to 800 °C under an energetic stirring for liquid homogenisation. Then, the melts were degassed using C_2Cl_6 and the slag removed by mechanical methods. Al-10Mg and 0.2 % Al-5Ti-1B master alloys were added into the melts under mechanical stirring to reduce the Mg loss in the alloys. The average size of TiB_2 particles in the Al-5Ti-1B master alloys is 0.77 ± 0.28 μm [21]. Finally, the melts were poured into a preheated steel mould (see Fig. 1) at 750 °C. During the solidification process, the cooling curves were recorded in the centre of the ingots. 8 alloys were prepared: 0.7Fe+Al-Ti-B, 1.2Fe+Al-Ti-B, 0.7Fe+USMP, 0.7Fe+Al-Ti-B+USMP, 1.2Fe+USMP, 1.2Fe+Al-Ti-B+USMP that are termed as 0.7FeB, 1.2FeB, 0.7FeU, 0.7FeUB, 1.2FeU, 1.2FeUB, respectively, for simplicity. The chemical composition of the studied alloys was analysed by optical spectrometry, and the results are summarized in Table 1.

2.2. Ultrasonic melt processing

The ultrasonic equipment is made up of an ultrasonic generator (1 kW), an magnetostrictive transducer (18 KHz) and an ultrasonic sonotrode (Ti-6Al-4V horn diameter: 30 mm). The schematic diagram of the ultrasonic melt processing setup is shown in Fig. 1a. During the experiment, the sonotrode was preheated to 400 °C using the electric-resistance coil to reduce the chilling effect. The sonotrode was inserted 30 mm into the melt at 710 °C, 5 min after the ultrasonic treatment, the melt temperature is about 695 °C. At this temperature, the melt is fully liquid, as the liquidus temperature of these two alloys are both about 640 °C. After that, the sonotrode was withdrawn from the melt and the crucible was extracted from the furnace for casting (Fig. 1b). Also, a thermocouple located in the centre of mould was used to record the cooling curves during solidification. The samples were cut using wire electrical discharge machining at the bottom of the ingot (Fig. 1c), and the size of the different samples is also schematic displayed in Fig. 1c).

2.3. Microstructural analysis

The metallographic samples (size: $7 \times 7 \times 7$ mm^3) were cut from the bottom of the ingots and prepared by standard grinding, polishing, and etching processes. Optical microscope (LEICA/DMI5000M, Germany) was used to analysis the microstructure of the casting alloys. A SEM (Sigma 500, Zeiss, Germany) combined with an energy-dispersive spectrometer (EDS, Oxford) was used to observe the microstructure and identify the phases present in the alloys. The 3D morphology of the
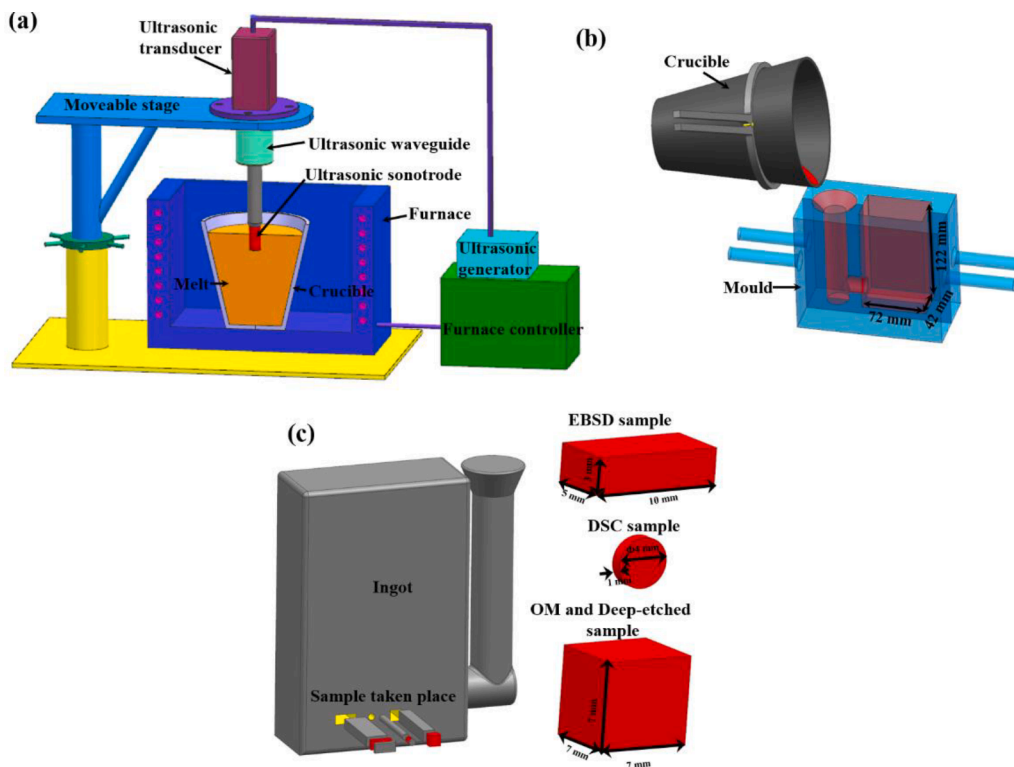
Fig. 1. Schematic diagram of (a) the ultrasonic melt treatment process; (b) casting process; (c) the sample position taken from the ingots.

Table 1
Chemical composition of the studied alloys (wt.%).

Designed Alloy	Cu	Mn	Fe	Mg	Si	Ti	Al
0.7Fe	4.66	0.54	0.60	0.50	0.22	–	Bal.
0.7FeB	4.58	0.54	0.57	0.50	0.26	0.22	Bal.
1.2Fe	4.41	0.52	1.08	0.49	0.21	–	Bal.
1.2FeB	4.42	0.53	1.15	0.50	0.28	0.19	Bal.
0.7FeU	4.60	0.52	0.72	0.57	0.04	0.13	Bal.
0.7FeUB	4.30	0.52	0.70	0.57	0.19	0.14	Bal.
1.2FeU	4.52	0.50	1.18	0.60	0.15	0.13	Bal.
1.2FeUB	4.31	0.53	1.21	0.57	0.19	0.14	Bal.

Fe-rich phases was revealed by methanol and solid iodine solution used to remove the Al matrix for 3–6 h. 30 binarized optical images were used to calculate the Fe-rich phases average size. The EBSD maps and Kikuchi patterns were measured using a sample-to-detector distance of ~ 10 mm and a voltage of 20 kV at the SEM. The sample was tilted 70° with respect to the detector. The scanning step size was set at 1 μm. The conventional procedure of counting grain boundaries in vertical and horizontal lines was used to calculate the average grain size. The samples were heated at a constant heating rate from 25 °C to 700 °C in DSC (Netzsch DSC 404, Germany) and then a constant cooling rate (10 °C/min) to 25 °C with the protection of Ar gas.

2.4. Thermodynamic calculation

The solidification sequences of 0.7Fe and 1.2Fe alloys were calculated by using the Scheil model in Thermo-Calc software. The results are shown in Fig. 2. In 0.7Fe alloy (Fig. 2a), the solidification sequences are: 1) L → α-Al; 2) L → α-Al + Al$_3$(FeMn); 3) L → α-Al + Al$_3$(FeMn) + Al$_6$(FeMn); 4) L → α-Al + Al$_6$(FeMn); 5) L → α-Al + Al$_6$(FeMn) + Al$_7$Cu$_2$Fe (β-Fe); 6) L → α-Al + β-Fe; 7) L → α-Al + Al$_6$(FeMn) + β-Fe + Al$_{15}$Fe$_3$Si$_2$(α-Fe); 8) L → α-Al + α-Fe; 9) L → α-Al + α-Fe + Al$_2$Cu; 10) L → α-Al + α-Fe + Al$_2$Cu + Mg$_2$Si; 11) L → α-Al + α-Fe + Al$_2$Cu + Mg$_2$Si + Al$_2$CuMg (S). The β-Fe and S phases are not detected in the alloys due to

the low content. In 1.2Fe alloy (Fig. 2b), the solidification sequences are similar to that of the 0.7Fe alloy except for the primary Al$_3$(FeMn) phases. So, the individual phase transformation for 0.7Fe alloy is: L → α-Al + Al$_3$(FeMn) + α-Fe + β-Fe + Al$_2$Cu + Mg$_2$Si + Al$_2$CuMg; for 1.2Fe alloy is: L → α-Al + Al$_3$(FeMn) + Al$_6$(FeMn) + β-Fe + Al$_2$Cu + Mg$_2$Si + Al$_2$CuMg. Fig. 2c shows the vertical section of Al-4.5Cu-0.5Mn-0.5Mg-0.2Si-xFe (x = 0–2) alloys, which demonstrates that the high Fe content promotes the formation of Al$_3$Fe phases. Table 2 shows the solidification sequences of 0.7Fe and 1.2Fe alloys obtained from the thermodynamic calculation (Fig. 2a and b). The Scheil solidification sequences obtained from the thermodynamic calculation are listed in Table 2.

3. Results

3.1. α-Al grain size

The EBSD maps along the x direction in the studied alloys and the inverse pole figures (IPF), are shown in Fig. 3. It can be seen that the conventional casting alloys exhibit a dendritic morphology, while the alloy with Al-Ti-B present a certain grain refinement effect. It is worth nothing that USMP process produces an equiaxial and uniform fine grain structure (Fig. 3c and d). Moreover, the combined USMP and Al-Ti-B method exhibits the most grain refinement effect. This is in accordance with Ref. [64]. The mean grain size in 0.7Fe, 0.7FeB, 0.7FeU, and 0.7UB alloys are 118.5, 101.0, 65.7, and 46.0 μm, respectively. In the USMP process, a gradient of grain sizes is found from the horn to the bottom of the ingot. After USMP processing, the melt was not directly solidified in the clay crucible, but poured into the steel mould. So, we assumed that the melt is homogenously and samples are taken at the bottom place. An increase in Fe content from 0.7 % to 1.2 % increases the mean grain size, Fig. 3. This indicates that USMP is an effectively method for grain refinement, the higher refinement is found in the 1.2Fe alloy.
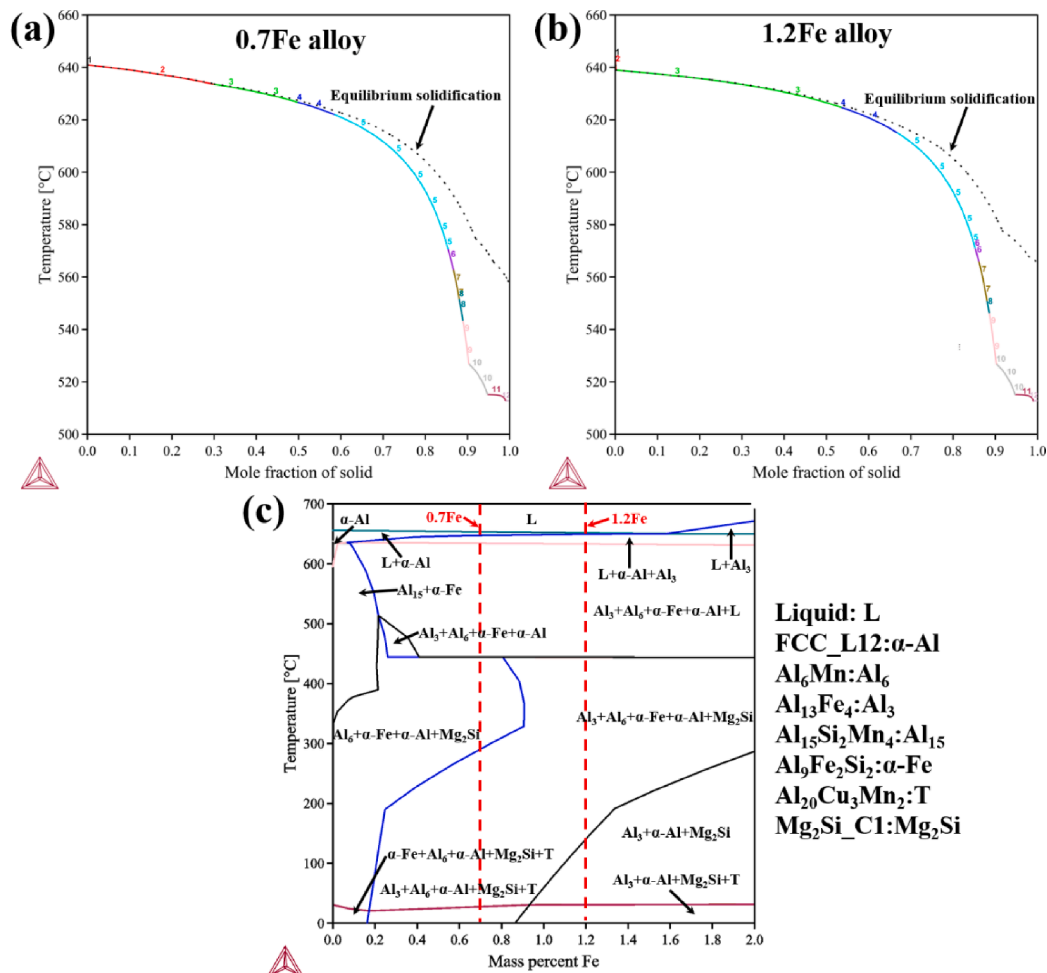
Fig. 2. The solidification sequences of different alloys calculated using Thermo-Calc software:(a) 0.7Fe alloy; (b) 1.2Fe alloy; (c) the vertical section of Al-4.5Cu-0.5Mn-0.5Mg-0.2Si-xFe (x = 0–2) alloys.

Table 2
The Scheil solidification sequences obtained from the thermodynamic calculation.

	0.7Fe alloy	1.2Fe alloy
1	L	L
2	L → α-Al	L → Al₃Fe
3	L → α-Al + Al₃Fe	L → α-Al + Al₃Fe
4	L + Al₃Fe → α-Al + Al₆Fe	L + Al₃Fe → α-Al + Al₆Fe
5	L → α-Al + Al₆Fe	L → α-Al + Al₆Fe
6	L + Al₆Fe → α-Al + β-Fe	L + Al₆Fe → α-Al + β-Fe
7	L → α-Al + β-Fe	L → α-Al + β-Fe
8	L + β-Fe → α-Al + α-Fe	L + β-Fe → α-Al + α-Fe
9	L → α-Al + α-Fe	L → α-Al + α-Fe
10	L → α-Al + α-Fe + Al₂Cu	L → α-Al + α-Fe + Al₂Cu
11	L → α-Al + Mg₂Si + Al₂Cu	L → α-Al + Mg₂Si + Al₂Cu
12	L → α-Al + Mg₂Si + Al₂Cu + Al₂CuMg	L → α-Al + Mg₂Si + Al₂Cu + Al₂CuMg

Row 2: $L \rightarrow \alpha\text{-Al}$; $L \rightarrow Al_3Fe$
Row 3: $L \rightarrow \alpha\text{-Al} + Al_3Fe$
Row 4: $L + Al_3Fe \rightarrow \alpha\text{-Al} + Al_6Fe$
Row 5: $L \rightarrow \alpha\text{-Al} + Al_6Fe$
Row 6: $L + Al_6Fe \rightarrow \alpha\text{-Al} + \beta\text{-Fe}$
Row 7: $L \rightarrow \alpha\text{-Al} + \beta\text{-Fe}$
Row 8: $L + \beta\text{-Fe} \rightarrow \alpha\text{-Al} + \alpha\text{-Fe}$
Row 9: $L \rightarrow \alpha\text{-Al} + \alpha\text{-Fe}$
Row 10: $L \rightarrow \alpha\text{-Al} + \alpha\text{-Fe} + Al_2Cu$
Row 11: $L \rightarrow \alpha\text{-Al} + Mg_2Si + Al_2Cu$
Row 12: $L \rightarrow \alpha\text{-Al} + Mg_2Si + Al_2Cu + Al_2CuMg$

3.2. Optical microscope

Fig. 4 shows the OM images of the studied alloys under different manufacturing conditions. In the conventional alloys, dark-grey Fe-rich phases, white Al₂Cu phases and medium-grey Mg₂Si phases are distributed in the interdendritic regions. In the conventional alloys, the Fe-rich phases exhibit the Chinese-script and coarse structures (Fig. 4a and b). Al-Ti-B addition partially changed the morphology of Fe-rich phases to blocky or plate-like structures (Fig. 4c and d, as indicated by red arrows). This indicates that Al-Ti-B not only affects the grain size of

α-Al, but also change the shape of Fe-rich phases. The USMP promotes a higher dispersion of Fe-rich phases (Fig. 4e and f). Moreover, the combined of USMP + Al-Ti-B process significantly refined the size of Fe-rich phases compared with individual processes (Fig. 4g and h).

3.3. Phase identification

The identification of Fe-rich phases by their morphology can be misleading in some cases, as for example Al₆(FeMn) and α-Fe. Thus, EDS mapping, point analysis, and Kikuchi patterns were used to identify these phases. The EDS element mapping of the four alloys produced without USMP are illustrated in Fig. 5. Fig. 5a shows the element distributions of Mg and Si (indicated by white circles). This phase is confirmed as Mg₂Si, which coincide with the SEM analysis and thermodynamic calculations (Fig. 2). Also, traces of Si exist in the Al₂Cu precipitates (see Fig. 5a-d). In addition, both the red and white dotted lines indicate the presence of Fe, but Si is only present in the region indicated by the red dotted line (Fig. 5a). The phase without Si is supposed to be Al₆(FeMn), Fig. 5a. The phase with Si is confirmed to be α-Fe according to the element mapping [18]. In addition, the AlSiTi phase is found in the 0.7FeB alloy (Fig. 5b), which is consistent with the results shown in [39]. In the 1.2Fe alloy (Fig. 5c), Mg₂Si (yellow dotted line) is also found through the coupled eutectic reaction with the Al₂Cu phase. Similarly, the Fe-rich phases with and without Si are identified as α-Fe (white circle) and Al₆(FeMn) respectively. In the 1.2FeB alloy (Fig. 5d), the Ti-containing particles are located in the Fe-rich phases, which allows to speculate that TiB₂ particles are pushed into the
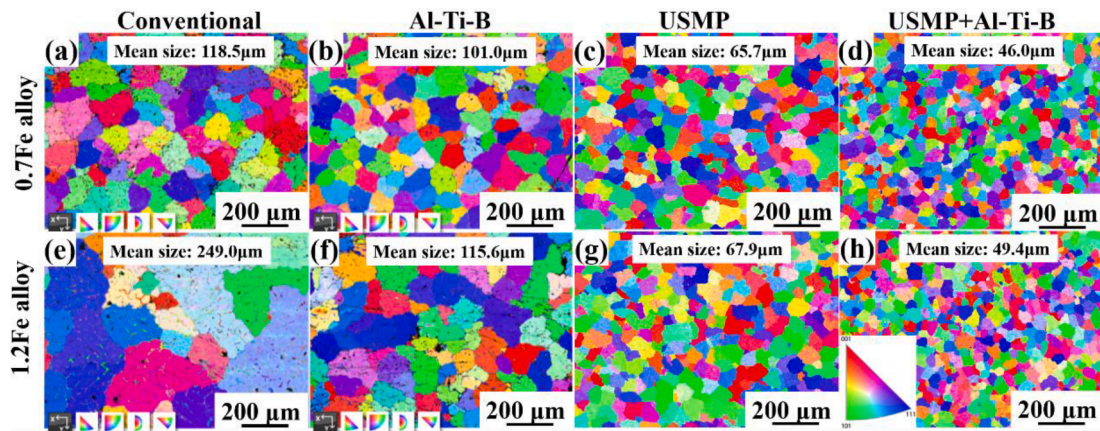
Fig. 3. The EBSD images and α-Al size distribution of different alloys: (a) 0.7Fe alloy; (b) 0.7FeB alloy; (c) 0.7FeU alloy; (d) 0.7FeUB alloy; (e) 1.2Fe alloy; (f) 1.2FeB alloy; (g) 1.2FeU alloy; (h) 1.2FeUB alloy.
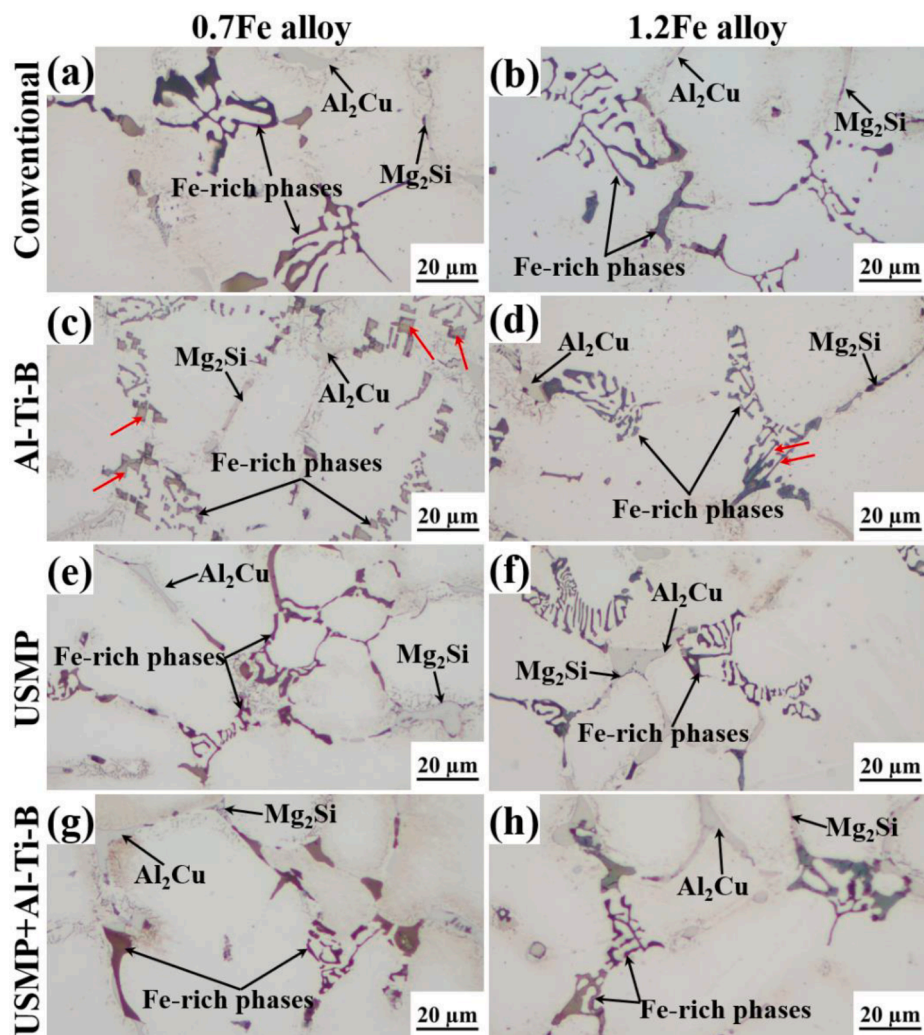

Fig. 4. OM images of the alloys: (a) 0.7Fe alloy; (b) 1.2Fe alloy; (c) 0.7FeB alloy; (d) 1.2FeB alloy; (e) 0.7FeU alloy; (f) 1.2FeU alloy; (g) 0.7FeUB alloy; (h) 1.2FeUB alloy.

interdendritic regions serving as heterogenous nucleation sites for Al$_3$(FeMn) phases [19,20].

The EDS element mapping of the two alloys with USMP are shown in Fig. 6. In 0.7Fe alloys, Fig. 6a and b, the presence of Mg$_2$Si (white circle) together with Al$_2$Cu is observed. The addition of Al-Ti-B does not modify the type of Fe-rich phases (Fig. 6b). In addition, some Si aggregates are found solubility into Al$_2$Cu particles (red dotted line), which is agreed with our previous studies [15,16]. The Ti containing particles (red circle) are located at the Al matrix, in accordance to the well accepted idea that the TiB$_2$ particles serve as heterogenous nucleation sites for α-Al.
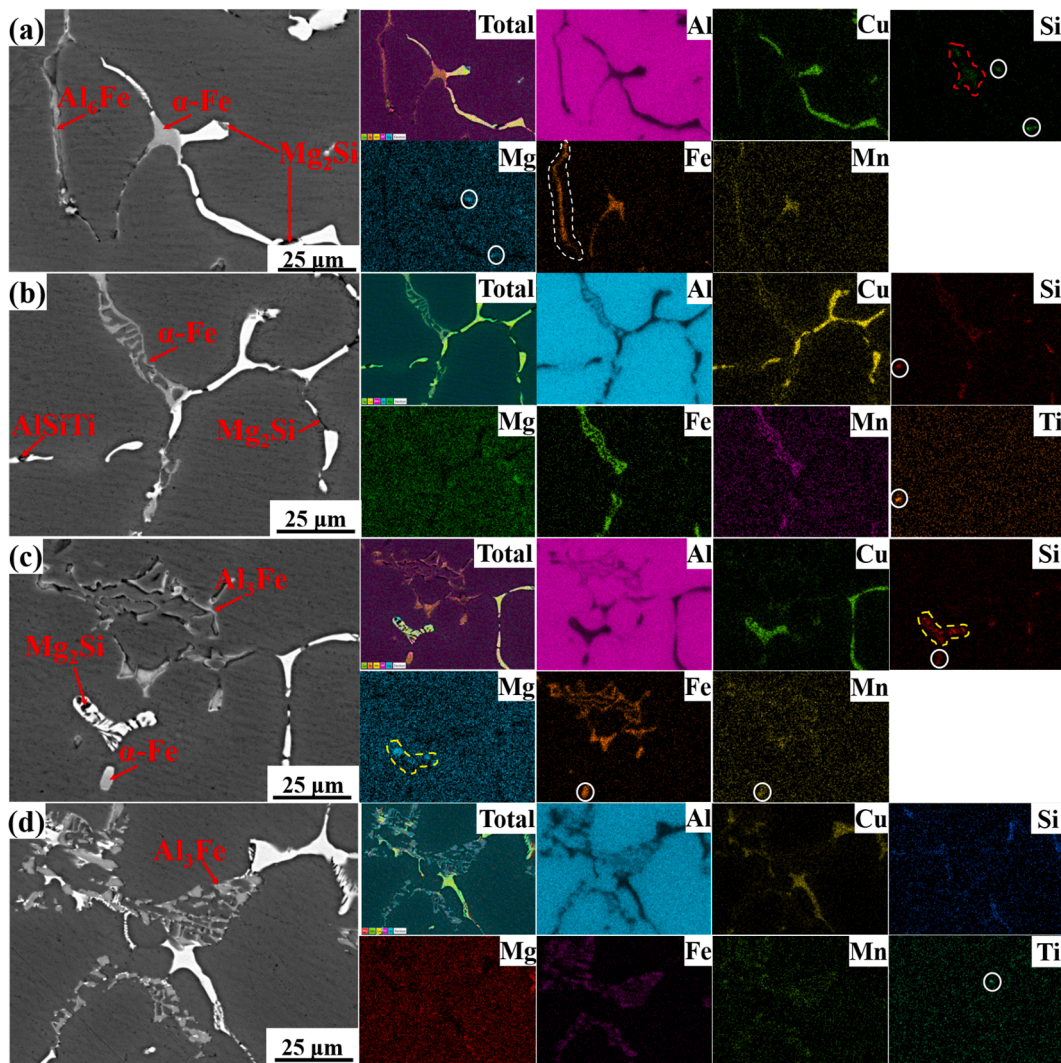
Fig. 5. SEM images and EDS element mapping of the alloys without USMP: (a) 0.7Fe alloy; (b) 0.7FeB alloy; (c) 1.2Fe alloy; (d) 1.2FeB alloy.
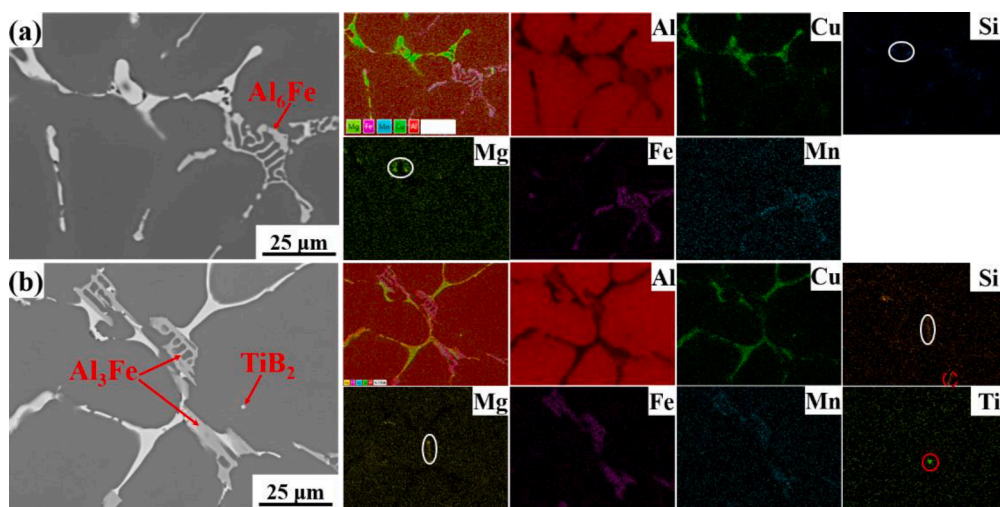

Fig. 6. The SEM images and EDS element mapping of the alloys with USMP: (a) 0.7FeU alloy; (b) 0.7FeUB alloy.

USMP is an efficient method for reduce the segregation of TiB_2 particles and promotes their heterogenous nucleation.

The identification of the type of intermetallic phases even with a combination of techniques as OM + SEM + EDS mapping, is very hard for some specific phases. Therefore, EBSD maps and Kikuchi patterns (Fig. 7) had been used to identify these Fe-rich phases. Al_3(FeMn) is
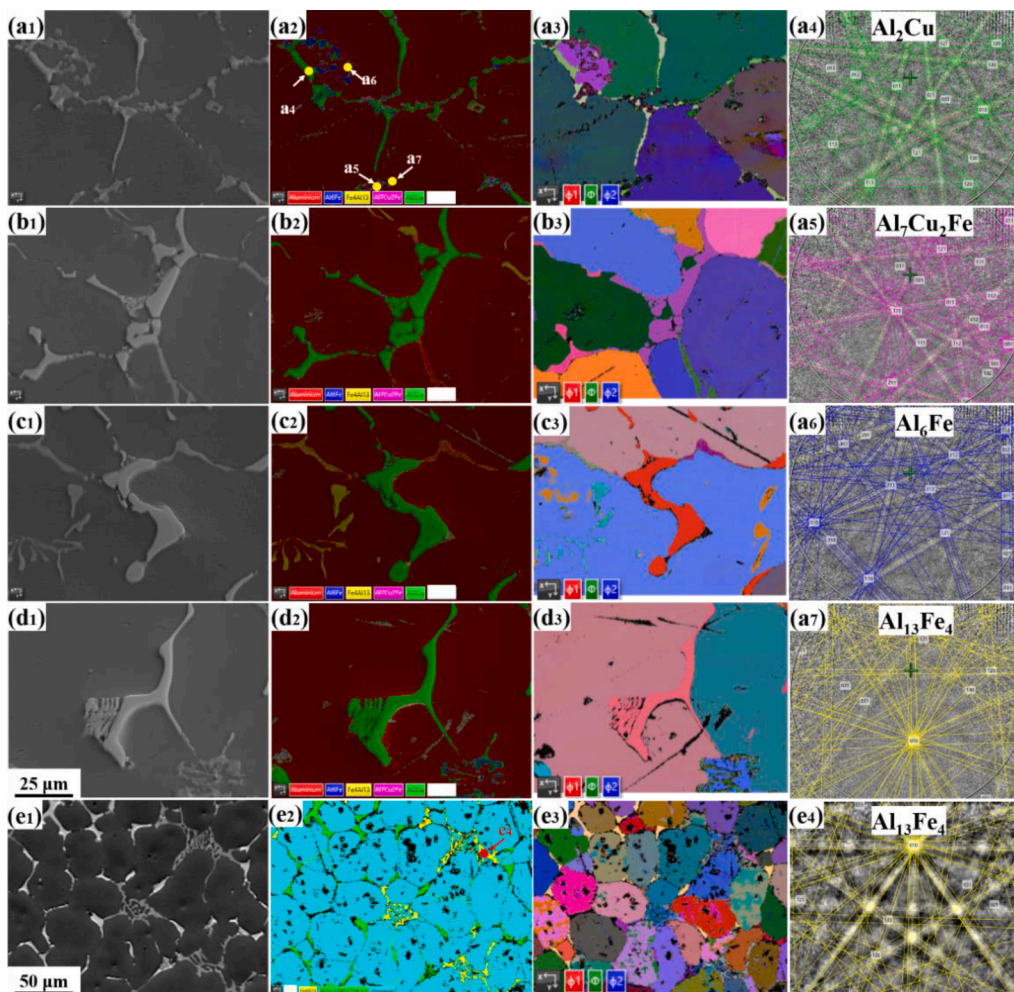
Fig. 7. SEM images and EBSD phase mapping, Kikuchi patterns of different phase in the studied alloys: (a₁-a₃) 0.7Fe alloy; (b₁-b₃) 0.7FeB alloy; (c₁-c₃) 1.2Fe alloy; (d₁-d₃) 1.2FeB alloy; (e₁-e₃) 1.2FeUB alloy; (a₄-a₇, e₄) Kikuchi patterns of different Fe-rich phases.

observed in the 0.7Fe and 1.2FeB alloys, Fig. 7a and d. However, as shown in Fig. 7b and c, $Al_6(FeMn)$ is observed in the 0.7FeB and 1.2Fe alloys. The $Al_3(FeMn)$ phases are also found in the 1.2FeUB alloy (Fig. 7e). The experimental Kikuchi patterns in Fig. 7a2 are shown in Fig. 7a4-7. The Al_2Cu (MAD = 0.38, 95.3, 124.9, 37.8), Al_7Cu_2Fe (MAD = 0.81, 40.1, 63.2, 22.5), $Al_6(FeMn)$ (MAD = 0.54, 108.1, 34.8, 90.8), and $Al_3(FeMn)$ (MAD = 0.99, 69.0, 119.2, 230.8) phases are identified in the alloys.

3.4. Solidification sequences of the studied alloys

The solidification sequences of the studied alloys under different solidification conditions were analysed by DSC and cooling curves. Fig. 8 shows the effect of the Fe content on the DSC cooling curve. There are 5 exothermic peaks both in 0.7 % and 1.2 %Fe alloys. These peaks correspond to the formation of α-Al, $Al_3(FeMn)/Al_6(FeMn)$, β-Fe/α-Fe, Al_2Cu, and Mg_2Si, respectively. In 0.7Fe alloy, the primary α-Al phases nucleated at 635 °C, followed by the peaks of $Al_3(FeMn)/Al_6(FeMn)$ and β-Fe/α-Fe at 617 °C and 552 °C, respectively. Finally, the Al_2Cu, and Mg_2Si peaks appear at 517 °C and 509 °C, respectively. The USMP process and the addition of Al-Ti-B, both slightly modify the formation temperatures of the different phases. Such as, the formation temperatures of α-Al, $Al_6(FeMn)$, Al_2Cu, and Mg_2Si increase by 4, 4, 4, and 1 °C, respectively. In the 1.2Fe alloys, the formation temperatures of α-Al, $Al_3(FeMn)$, $Al_6(FeMn)$, Al_2Cu, and Mg_2Si are 637, 625, 559, 513, and 508 °C, respectively. Furthermore, the Al-Ti-B addition and USMP in 1.2

%Fe alloy also modify the intermetallic formation temperatures. The formation temperatures of the intermetallic phases generated in different conditions are summarized in Table 3.

The cooling curves taken during solidification are shown in Fig. 9. The formation temperatures are obtained from the first-order derivative of the cooling curves. As can be seen in Fig. 9, the maximum under-cooling of α-Al is greatly reduced by the Al-Ti-B addition and USMP both in the 0.7Fe and 1.2Fe alloys. Such as, the formation temperature of α-Al in 1.2Fe alloy is 636 °C; while this temperature in the 1.2FeU alloy is 649 °C. The primary α-Al phase nucleation temperature under USMP is not clearly in the recorded cooling curves. This is due to the USMP temperature is 710 °C and the melt temperature is about 695 °C after 5 min. The melt temperature is close to the liquidus temperature when the melt was poured into the steel mould. The first-order derivative of the cooling curves also shows five exothermic peaks corresponding to the five solidification reactions (Fig. 9c). Fig. 9d shows the schematic diagram used to calculate the nucleation temperature of the different phases. It is also evidenced that the heterogeneous nucleation of TiB_2 and the strong effect of acoustic streaming and cavitation affect the formation temperatures of Fe-rich phases, Al_2Cu and Mg_2Si. The nucleation temperature of different phases measured by DSC and cooling curve are presented in Table 3. Based on the above analysis of DSC (Fig. 8) and cooling curves (Fig. 9), the possible solidification reactions for both alloys are listed in Table 4.

In order to study the effect of USMP + Al-Ti-B process on the Fe-rich phases size in different alloys, the area of single Fe-rich phases is shown
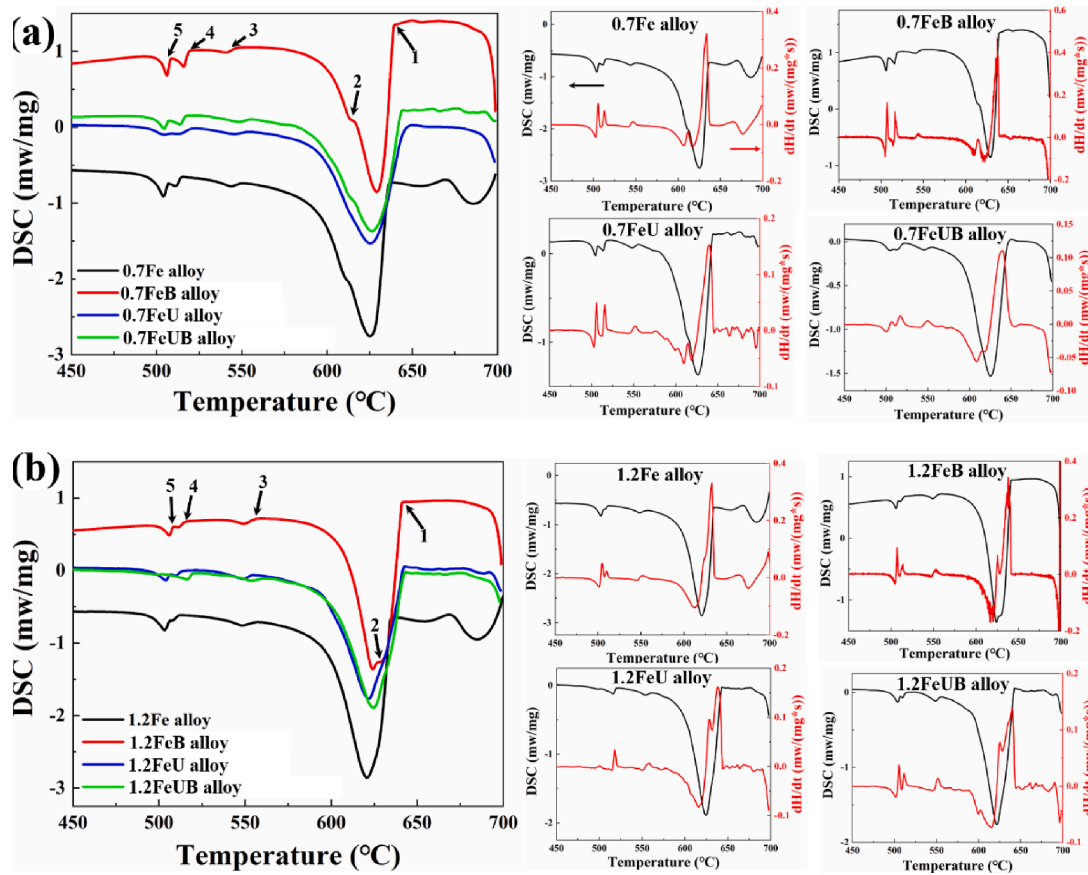
Fig. 8. The DSC cooling curve (10 °C/min) of different alloys under different conditions: (a) 0.7Fe alloy; (b) 1.2Fe alloy.

Table 3
The nucleation temperature of different phases measured by DSC (Fig. 8) and cooling curve (CC) (Fig. 9). (Unit: °C).

Alloy	Peak 1		Peak 2		Peak 3		Peak 4		Peak 5	
	DSC	CC	DSC	CC	DSC	CC	DSC	CC	DSC	CC
0.7Fe	635	642	617	616	552	577	517	519	509	511
0.7FeB	640	–	620	613	549	581	521	516	510	510
0.7FeU	646	644	619	617	557	–	520	515	512	511
0.7FeUB	654	–	619	618	560	–	524	522	511	513
1.2Fe	637	636	625	629	559	558	513	518	508	508
1.2FeB	642	643	628	631	561	–	517	519	509	512
1.2FeU	644	649	628	633	563	–	522	525	505	505
1.2FeUB	644	–	631	636	556	571	516	515	508	507

in Fig. 10. The image binarization in OM images were conducted according to their colour, Fig. 10 a and b. The binarization process was performed by the ImageJ software. The total threshold value is 0–255, the criteria for Fe-rich phases (white colour) is 93–255. The area size distributions are shown in Fig. 10 c and d. At least 30 images were used for the statistical analysis. Hence, the USMP + Al-Ti-B process refine the size of single Fe-rich particles in comparison with individual methods.

The 3D morphology of Fe-rich phases is also influenced by the Fe content and processing methods of the studied alloys, as demonstrated in Fig. 11. In conventional casting sample (Fig. 11a and e), coarse and fine dendritic Fe-rich phases are observed. As shown in Fig. 11b and c, the Fe-rich phases in 0.7FeB and 0.7FeU alloys are better dispersed. In Fig. 11d, it is shown that the size of Fe-rich phases in 0.7FeUB alloy is refined compared with individual methods. However, the morphology of Fe-rich phases in 1.2Fe alloys is more disperse with skeleton structure (Fig. 11e-h).

4. Discussions

4.1. Effect of USMP and Al-Ti-B on grain size of the studied alloys

It is universally acknowledged that the Al-Ti-B grain refiner have a good grain refinement of α-Al, as TiB₂ particles can serve as heterogeneous nucleation sites for α-Al [66,67]. The solute element, and melt process parameters have a strong influence on alloy's grain size. The growth restriction factor (GRF) is calculated by Equation (1), Q represent the growth restriction degree obtained for a multiphase alloy upon solidification [68].

$$Q = \sum_j m_j(k_j - 1)C_j \tag{1}$$

where m_j is the liquidus line slope on the different equilibrium binary phase diagram, and k_j are the equilibrium distribution coefficient and C_j is the solute concentration of element j, respectively. The value of liquidus line slope (m_j) and equilibrium distribution coefficient (k_j) for
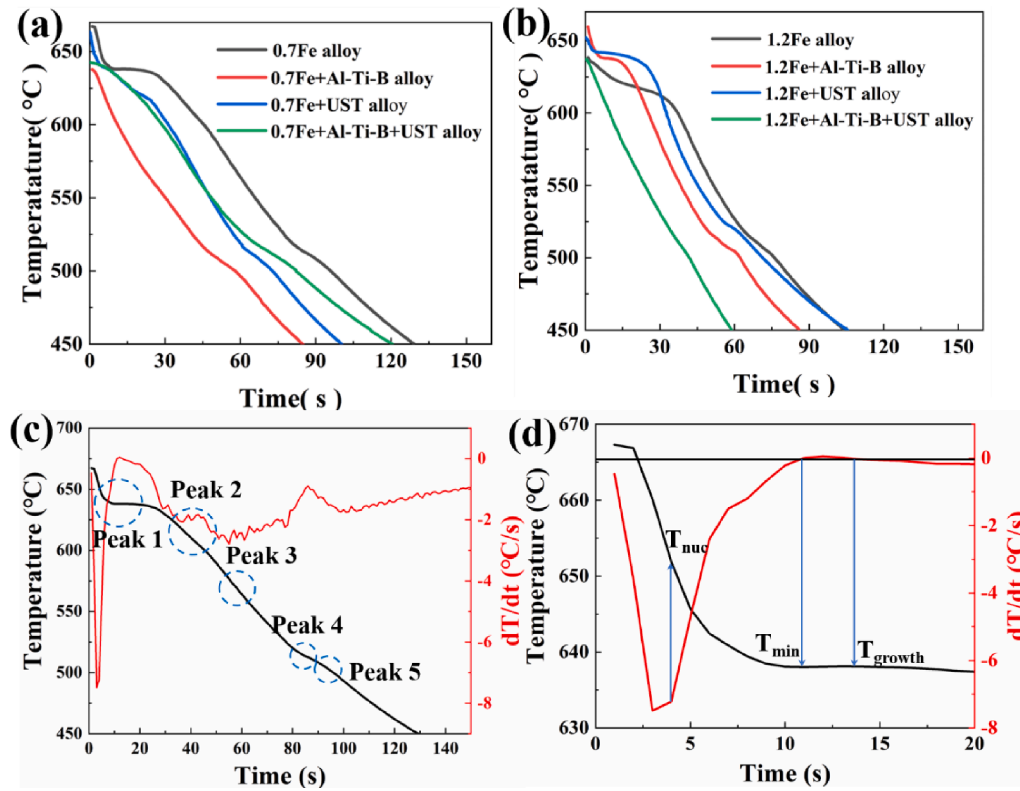
Fig. 9. The cooling curve measured during solidification of different alloys: (a) 0.7Fe alloy; (b) 1.2Fe alloy; (c) the first-order derivative of the cooling curves; (d) the schematic diagram used to calculate the nucleation, undercooling and growth temperature.

Table 4
The possible solidification reactions in the studied alloys.

	Reactions	Temperature range (°C)
1	L → α-Al / L → Al₃(FeMn)	635–654
2	L → α-Al + Al₃(FeMn)/Al₆(FeMn)	613–631
3	L + Al₃(FeMn)/Al₆(FeMn) → α-Al + β-Fe/α-Fe	548–580
4	L → α-Al + β-Fe + Al₂Cu	513–524
5	L → α-Al + Al₂CuMg + Al₂Cu + Mg₂Si	504–513

different elements are listed in Table S1.

The relationship between the grain size (d) and $1/Q$ in solidified alloys with and without USMP is calculated by equation [69]:

$$d = a + b * 1/Q \tag{2}$$

where a and b are constants. The values of $1/Q$ in the 0.7Fe, 0.7FeB, 0.7FeU, and 0.7FeUB alloys are 0.056, 0.013, 0.054, and 0.015, respectively; and the calculated d is 118.5, 101.0, 65.7, 46.0 um, respectively. The relationship between $1/Q$ and grain size of the studied alloys are plotted in Fig. 12. A clear contribution of the UMSP and Al-Ti-B addition contribution to the grain refinement can be seen in Fig. 12. However, the combination of UMSP and Al-Ti-B have a better grain refinement efficiency, with the 0.7Fe alloy presenting the smallest grain size. An increase in the Fe content from 0.7 % to 1.2 % increases the grain size. The specific relations found in the present case are d = 87 + 1000*1/Q for alloys with USMP, and d = 37 + 537*1/Q for alloys without USMP (see Fig. 12).

It is interesting to note that the USMP process have a higher refinement efficiency compared to Al-Ti-B. This is due to the agglomeration tendency of TiB₂ particles in the Al melts [19,20], that greatly decreases their grain refinement efficiency. It is widely accepted that the USMP process produces the effects of acoustic cavitation and acoustic streaming. The ultrasonic intensity I is calculated by [43,44]:

$$I = \frac{1}{2} * \rho c (2\pi f A)^2 \tag{3}$$

The density ρ of molten Al at 700 °C is 2.4 kg/m³, the sound velocity c in liquid Al at 700 °C is 4.6×10^3 m/s, the ultrasonic vibration frequency f is 20 kHz and the applied amplitude A is estimated to be 20 μm. Thus, the calculated ultrasonic intensity I in the current study is approximately 875 W/cm², which is higher than the threshold value required producing acoustic cavitation in molten Al (100 W/cm²) [44].

USMP is one of the most effective methods for grain refinement during solidification of alloys [44,45]. Various mechanisms have been established based on the *in-situ* studies [46–48] and post-mortem experiments [49–52] to justify its influence on alloy refinement. The different refinement mechanisms are mainly related to the melt temperature: 1) above the liquidus temperature and 2) temperature between liquidus and solid temperature (semi-solid temperature zone). When the melt temperature is above the liquidus temperature, the cavitation-enhanced grain nucleation and cavitation-enhanced inclusion nucleation are the two main mechanisms [44,46]. When the cavitation bubbles reach the negative pressure, the bubbles will implosion and generate a very high local pressure (up to several GPa). The pressure will be resulting in the high local undercooling, which facilitates the solid nucleus generation and promotes the homogenous nucleation. This is the main mechanism for grain refinement. Moreover, the cavitation improves the wetting of inclusions (so-called sonocapillary effect), which promote these inclusions for heterogenous nucleation sites for primary α-Al phases. The second mechanism of the grain refinement is cavitation induced-dendrite fragmentation in the semi-solid temperature zone. After the primary phases are formed, the cavitation bubbles continually attacked the growing dendrite phases and resulting in the fatigue fracture. These fragment dendrites will be grown up as the new grains. This phenomenon had been clearly observed by the high-speed synchrotron X-ray imaging [45–47].

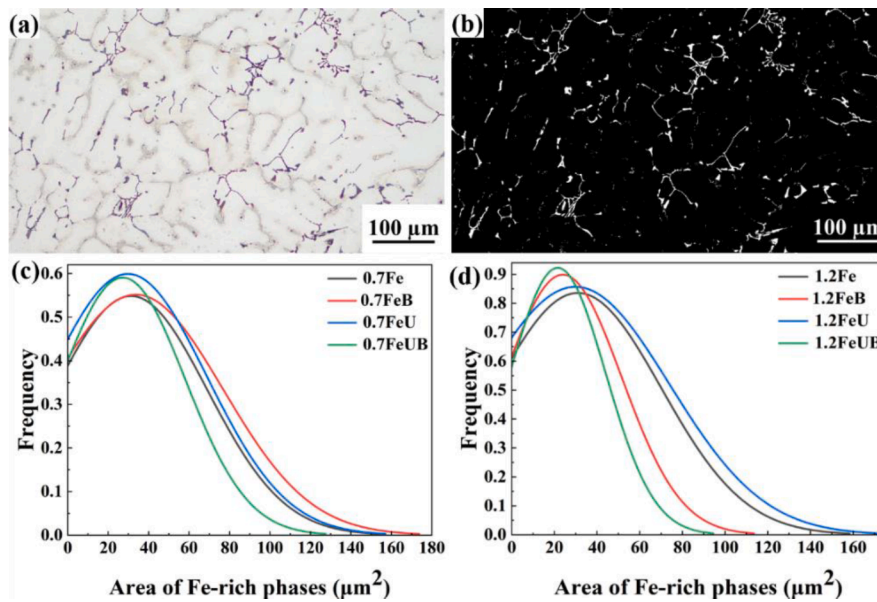In the present case, the USMP temperature for both melts are 710 °C,

Fig. 10. Example of Fe-rich phases distribution images: (a) original image; (b) binarized image (The threshold value, 93–255, has been determined by ImageJ software). The area of Fe-rich phases under different conditions: (c) 0.7Fe alloys; (d) 1.2Fe alloys.
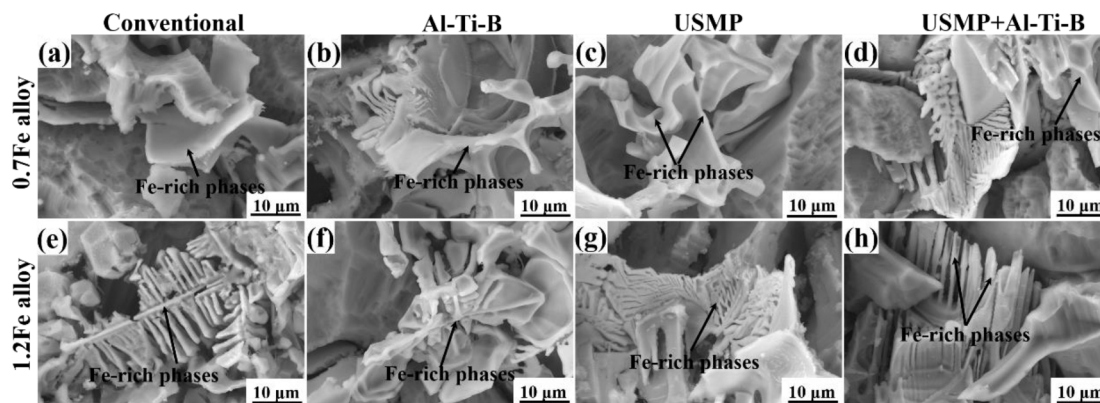

Fig. 11. The deep-etched morphologies of Fe-rich phases in different alloys: (a, e) conventional alloy; (b, f) Al-Ti-B alloy; (c, g) USMP alloy; (d, h) USMP + Al-Ti-B alloy; (a-d) 0.7Fe alloy; (e-h) 1.2Fe alloy.
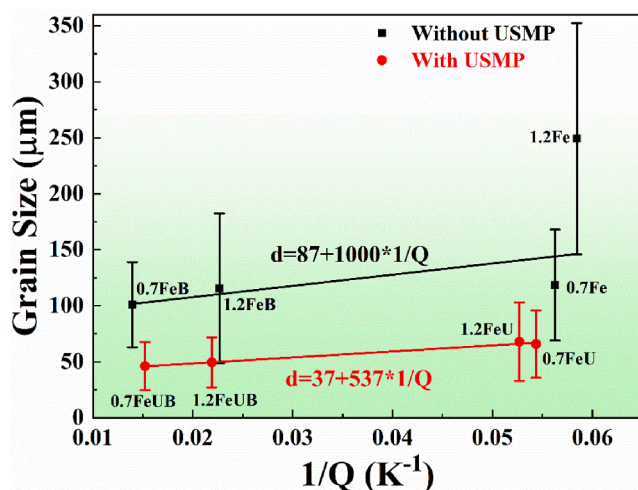

Fig. 12. The relationship between the grain size and 1/Q in alloys solidified without and with USMP.

which is higher than the liquidus temperature of the alloys. This ensures that the USMP force the wetting of TiB$_2$ particles which is the main mechanisms for heterogenous nucleation. The bubbles generated by acoustic cavitation continuously broke the agglomerated TiB$_2$ clusters and the acoustic streaming homogeneously distributes these deagglomerated TiB$_2$ parties in the Al melts. Thus, the greater the heterogeneity in nucleation, the greater the decrease in the nucleation undercooling of α-Al (Table 2). For example, the nucleation temperature for α-Al in 0.7Fe alloy for the conventional alloy, with Al-Ti-B, USMP, and combined USMP and Al-Ti-B is 635, 640, 646, and 654 °C, respectively. Hence, both and USMP and Al-Ti-B reduce the nucleation undercooling similarly with the Ref. [65].

4.2. Effect of USMP and Al-Ti-B on the formation of Fe-rich phases

The Fe-rich phases in 0.7Fe and 1.2Fe alloys are formed through different solidification reaction, so USMP and Al-Ti-B have different effect on them. The refinement mechanism of Fe-rich phases is based on the melt temperature and solidification stage. As shown in Fig. 2, Al$_3$(FeMn), Al$_6$(FeMn) and α-Fe phases in 0.7Fe alloy are mostly formed through eutectic or peritectic reaction; while only a very small volume fraction of Al$_3$(FeMn) phases in 1.2Fe alloy are formed through prior to

the α-Al. The Fe-rich phases in different alloys are different. The calculated vertical section phase diagram of Al-4.5Cu-0.5Mn-0.5Mg-0.2Si-xFe (x = 0–2) alloys is presented in Fig. 2c. It can be seen that the Fe-rich phases are mostly formed through the eutectic reaction in 0.7Fe alloy; while a small proportion of primary $Al_3(FeMn)$ phases are formed in the 1.2Fe alloy and this can be ignored. So, we similarly regard that the 0.7Fe and 1.2Fe alloys have the same mechanism. The main refinement mechanism for Fe-rich phases is the 'liquid pocket' mechanism due to the refined interderdntic regions have narrow room for the eutectic reaction. As the Fe content increases, the percentage of $Al_3(FeMn)$ phase also increases. Due to the equilibrium phase diagram, the metastable $Al_6(FeMn)$ phases is not found in the system.

Fig. S3 presents the XRD patterns of the deep-etched 0.7Fe and 1.2Fe alloys with Al-Ti-B addition and USMP processing. The deep-etched process reduces the intensity of α-Al and increases the relative intensity of the intermetallic particles. It can be seen that α-Al, $Al_3(FeMn)$, $Al_6(FeMn)$, α-Fe, and Al_2Cu phases are co-existed in both 0.7Fe and 1.2Fe alloys. $Al_6(FeMn)$ and α-Fe are the main Fe-rich phases in 0.7Fe alloy, while relatively intensity of $Al_3(FeMn)$ and $Al_6(FeMn)$ are increased in 1.2Fe alloys. If the Fe content increases from 0.7 to 1.2 %, the type of Fe-rich phases does not change, the main Fe-rich phases change from $Al_6(FeMn)$ and α-Fe to $Al_3(FeMn)$ and $Al_6(FeMn)$. Moreover, the Al-Ti-B promotes the formation of $Al_3(FeMn)$ in 1.2Fe alloy, which is maybe due to the low crystal misfit between TiB_2 and $Al_3(FeMn)$ phases (Fig. 4c and d).

The size of the Fe-rich phases is greatly influenced by the USMP processing and the Al-Ti-B addition. The refined size of Fe-rich phases, Fig. 11, under USMP + Al-Ti-B is due to the formation of Fe-rich phases after the α-Al. The narrow and refined secondary interdendritic regions limit their growth. The refinement of Fe-rich phases is related to the α-Al grain size reduction in the studied processes. Due to the USMP temperature is above the its liquidus temperature, and wetting and deagglomerated TiB_2 particles induced by USMP are the main reason for dispersion of Fe-rich phases. For example, the nucleation temperature for $Al_3(FeMn)$ or $Al_6(FeMn)$ phases in 1.2Fe, 1.2FeB, 1.2FeU and 1.2FeUB alloys are 625, 628, 628, and 631 °C, respectively. This indicates that both USMP and Al-Ti-B increases the nucleation temperature of these Fe-rich phases and also, the USMP process deagglomerates the TiB_2 particles that are pushed into the liquidus/solid interface and subsequently engulfed into the residual liquid serving as heterogeneously distributed nucleation sites for Fe-rich phases. On the other hand, the nucleation rate around the location of collapsed cavitation bubbles would significantly increase. This reduces the critical nucleation radius and promote the nucleation rates.

Also, it should be mentioned that the USMP processing also influences shape and distribution of the Fe-rich in the Al alloys, Fig. 11. The acoustic streaming and bubbles generation by USMP process homogenize the solute elements and improves the Fe-rich phase dispersion. Also, TiB_2 particles in the Al-Ti-B-containing alloys act as heterogeneous nucleation sites for Fe-rich phases [20,21]. In the 0.7FeUB and 1.2FeUB alloys, the acoustic streaming uniformly distributes the TiB_2 particles and solutes elements, which promotes a heterogeneously nucleation in the narrow α-Al interdendritic region.

Finally, the 3D morphology and distribution of Fe-rich phases is also influenced by the Fe content and processing of the studied alloys, Fig. 11. The Fe-rich phases in 0.7FeB and 0.7FeU alloys are better dispersed, because the USMP disperse the Fe-rich phases and TiB_2 promotes a heterogeneous nucleation. However, the morphology of Fe-rich phases in 1.2Fe alloys is more disperse with skeleton structure (Fig. 11e-h) due to the high content of Fe in the residual liquid at the last solidification stage to form Fe-rich phases. Al-Ti-B increases the nucleation temperature of Fe-rich phases, providing them more space to growth and impinge. The acoustic bubbles induced by USMP can deagglomeration, and fragmentation the dendrite and intermetallic phases; acoustic streaming can wet the nucleate substrate and promote the nucleation. Acoustic streaming can promote the equiaxed crystal and reduces the

temperature gradient in the melt, in which the deagglomerates TiB_2 particles provided more effective nucleation sites for grain refinement. As the Fe content increases, Fe solute are rejecting into the interdendritic regions at the solid/liquid front resulting in constitutional undercooling, this also promotes the nucleation of Fe-rich phases.

5. Conclusions

The microstructural evolution during solidification of Al-4.5Cu-0.5Mn-0.5Mg-0.2Si-xFe alloys (x = 0.7, and 1.2 wt%) under gravity casting, USMP, Al-Ti-B and USMP + Al-Ti-B is comparatively studied by OM, SEM, EBSD, thermodynamic calculation, DSC, and thermal analysis. The main conclusions are listed as below:

1). The combination of USMP and Al-Ti-B methods produces a higher grain refinement effect compared with the individual methods. The main reason for refinement is that USMP deagglomerates the TiB_2 clusters, which providing more effective nucleation sites for α-Al. The averaged grain size is reduced by a 61 % in the 0.7Fealloy. In the 1.2Fe alloys, combined USMP and Al-Ti-B methods produce even a higher refinement effect (80 %).

2). The Fe-rich phases in both alloys with USMP + Al-Ti-B are refined and more homogenous distributed compared with conventional methods. As the USMP temperature is above the liquidus temperature of the studied alloys which generates the acoustic streaming during the process acting as the main refinement mechanism. The deagglomerated TiB_2 particles are pushed into the refined interdendritic regions limiting the growth of Fe-rich phases in the following eutectic reaction.

3). The acoustic cavitation produced by the USMP processing increases the equilibrium freezing point. This promotes the wetting of the TiB_2 particles providing heterogeneous nucleation sites. Moreover, the TiB_2 particles are the ideal nucleation sites for α-Al and unused TiB_2 particles are pushed into the interdentric regions and serves nucleation sites for Fe-rich phases.

CRediT authorship contribution statement

Yuliang Zhao: Conceptualization, Methodology, Investigation, Writing – original draft, Writing – review & editing, Funding acquisition, Project administration. **Weixiang He:** Methodology, Visualization, Investigation, Formal analysis, Data curation. **Dongfu Song:** Formal analysis, Investigation, Validation, Data curation. **Fanghua Shen:** Formal analysis, Data curation. **Xinxin Li:** Data curation, Formal analysis. **Zhenzhong Sun:** Resources. **Yao Wang:** Software. **Shuhong Liu:** Software. **Yong Du:** Software. **Ricardo Fernández:** Supervision, Formal analysis, Writing – review & editing, Resources.

Declaration of Competing Interest

The authors declare that they have no known competing financial interests or personal relationships that could have appeared to influence the work reported in this paper.

Data availability

Data will be made available on request.

Acknowledgement

for provision of synchrotron radiation beamtime. Y. Zhao thanks China Scholarship Council for providing financial support during the visiting in CENIM-CSIC, Spain.

Appendix A. Supplementary data

Supplementary data to this article can be found online at https://doi.org/10.1016/j.ultsonch.2022.106139.

References

[1] D. Raabe, D. Ponge, P. Uggowitzer, M. Roscher, M. Paolantonio, C. Liu, H. Antrekowitsch, E. Kozeschnik, D. Seidmann, B. Gault, F.D. Geuser, A. Dechamps, C. Hutchinson, C. Liu, Z. Li, P. Prangnell, J. Robson, P. Shanthraj, S. Vakili, C. Sinclair, L. Bourgeois, S. Pogatscher, Making sustainable aluminum by recycling scrap: the science of "dirty" alloys, Prog. Mater. Sci. 128 (2022), 100947.

[2] X. Lu, Z. Zhang, T. Hiraki, O. Takeda, H. Zhu, K. Matsubae, T. Nagasaka, A solid-state electrolysis process for upcycling aluminium scrap, Nature (2022).

[3] V.K. Soo, J.R. Peeters, P. Compston, M. Doolan, J.R. Duflou, Economic and environmental evaluation of aluminium recycling based on a Belgian case study, Procedia Manuf. 33 (2019) 639–646.

[4] K. Ganjehfard, R. Taghiabadi, M.T. Noghani, M.H. Ghoncheh, Tensile properties and hot tearing susceptibility of cast Al-Cu alloys containing excess Fe and Si, Int. J. Min. Met. Mater. 28 (2021) 718–728.

[5] H. Guo, W. Hu, K. Yang, C. Yu, Effects of Si and Fe additions on mechanical properties of as-cast Al-5Cu alloys, Mater. Sci. Tech. 38 (2022) 352–362.

[6] S. Fentazi, M. Bournane, K.A. Ragab, B. Mehdie, Influence of Mg additions on solidification and performance of B206-type aluminum castings of high Fe and Si contents, Inter. J. Cast Metal Res. 31 (2018) 14–17.

[7] H.K. Kamga, D. Larouche, M. Bournane, A. Rahem, Solidification of aluminum-copper B206 alloys with iron and silicon additions, Metall. Mater. Trans. A. 41 (2010) 2844–2855.

[8] J.D. Poplawsky, B.K. Milligan, L.F. Allard, D. Shin, P. Shower, M.F. Chisholm, A. Shyam, The synergistic role of Mn and Zr/Ti in producing θ'/L12 co precipitates in Al-Cu alloys, Acta Mater. 194 (2020) 577–586.

[9] T. Tancogne-Dejean, C.C. Roth, T.F. Morgeneyer, L. Helfen, D. Mohr, Ductile damage of AA2024-T3 under shear loading: Mechanism analysis through in-situ laminography, Acta Mater. 205 (2021), 116556.

[10] A.T. Kermanidis, Aircraft Aluminum Alloys: Applications and Future Trends, in S. Pantelakis, K. Tserpes (ed.), Revolutionizing Aircraft Materials and Processes, 2020, PP. 21-55.

[11] K. Hu, C. Lin, S. Xia, C. Zheng, B. Lin, Effect of Fe content on low cycle fatigue behavior of squeeze cast Al-Zn-Mg-Cu alloys, Mater. Charact. 170 (2020), 110680.

[12] K. Liu, X. Cao, X.G. Chen, Effects of iron-rich intermetallics on tensile deformation of Al-Cu 206 cast alloys, Metall. Mater. Trans. B 46B (2015) 1566–1575.

[13] K. Liu, X. Cao, X.G. Chen, Tensile properties of Al-Cu 206 cast alloys with various iron contents, Metall. Mater. Trans. A 45 (2014) 2498–2507.

[14] W. Zhang, B. Lin, D. Zhang, Y. Li, Microstructures and mechanical properties of squeeze cast Al–5.0Cu–0.6Mn alloys with different Fe content, Mater. Des. 52 (2013) 225–233.

[15] B. Lin, W. Zhang, Z. Lou, D. Zhang, Y. Li, Comparative study on microstructures and mechanical properties of the heat-treated Al–5.0Cu–0.6Mn–xFe alloys prepared by gravity die casting and squeeze casting, Mater. Des. 59 (2014) 10–18.

[16] Y.L. Zhao, W.W. Zhang, C. Yang, D.T. Zhang, Z. Wang, Effect of Si on Fe-rich intermetallic formation and mechanical properties of heat-treated Al-Cu-Mn-Fe alloys, J. Mater. Res. 33 (2018) 898–911.

[17] W.W. Zhang, Y.L. Zhao, D.T. Zhang, Z.Q. Luo, C. Yang, Y.Y. Li, Effect of Si addition and applied pressure on microstructure and tensile properties of as-cast Al-5.0Cu-0.6Mn-1.2Fe alloys, T. Nonferr. Met. Soc. 28 (2018) 1061–1072.

[18] W. Zhang, B. Lin, J. Fan, D. Zhang, Y. Li, Microstructures and mechanical properties of heat-treated Al–5.0Cu–0.5Fe squeeze cast alloys with different Mn/Fe ratio, Microstructures and mechanical properties of heat-treated Al–5.0Cu–0.5Fe squeeze cast alloys with different Mn/Fe ratio, Mater. Sci. Eng. A 588 (2013) 366–375.

[19] K. Liu, X. Cao, X.G. Chen, Effect of Mn, Si, and cooling rate on the formation of iron-rich intermetallics in 206 Al-Cu cast alloys, Metall. Mater. Trans. B 43 (2012) 1231–1240.

[20] Y. Zhao, D. Song, H. Wang, X. Li, L. Chen, Z. Sun, Z. Wang, T. Zhai, Y. Fu, Y. Wang, S. Liu, Y. Du, W. Zhang, Revealing the nucleation and growth mechanisms of Fe-rich phases in Al-Cu-Fe(-Si) alloys under the influence of Al-Ti-B, Intermetallics 146 (2022), 107584.

[21] Y.L. Zhao, W.W. Zhang, D.F. Song, B. Lin, F.H. Shen, D.H. Zheng, C.X. Xie, Z.Z. Sun, Y.N. Fu, R.X. Li, Nucleation and growth of Fe-rich phases in Al-5Ti-1B modified Al-Fe alloys investigated using synchrotron X-ray imaging and electron microscopy, J. Mater. Sci. Technol. 80 (2021) 84–99.

[22] Y.L. Zhao, B. Lin, D.F. Song, D.H. Zheng, Z.Z. Sun, C.X. Xie, W.W. Zhang, Effect of compound fields of ultrasonic vibration and applied pressure on the 3D microstructure and tensile properties of recycled Al-Cu-Mn-Fe-Si alloys, Materials 12 (2019) 3904.

[23] Y.L. Zhao, D.F. Song, B. Lin, C. Zhang, D.H. Zheng, S. Inguva, T. Li, Z.Z. Sun, Z. Wang, W.W. Zhang, 3D characterization of ultrasonic melt processing on the microstructural refinement of Al-Cu alloys using synchrotron X-ray tomography, Mater. Charact. 153 (2019) 354–365.

[24] H.R. Kotadia, M. Qian, A. Das, Microstructural modification of recycled aluminium alloys by high-intensity ultrasonication: observations from custom Al–2Si–2Mg–1.2Fe-(0.5,1.0)Mn alloys, J. Alloy. Compd. 823 (2020), 153833.

[25] J. Cao, S. Shuai, C. Huang, T. Hu, C. Chen, J. Wang, Z. Ren, 4D synchrotron X-ray tomographic study of the influence of transverse magnetic field on iron intermetallic compounds precipitation behavior during solidification of Al–Si–Fe alloy, Intermetallics 143 (2022), 107471.

[26] R.F. Gutiérrez, F. Sket, E. Maire, F. Wilde, E. Boller, G. Requena, Effect of solution heat treatment on microstructure and damage accumulation in cast Al-Cu alloys, J. Alloy. Compd. 697 (2017) 341–352.

[27] D. Xu, C. Zhu, C. Xu, K. Chen, Microstructures and tensile fracture behavior of 2219 wrought Al–Cu alloys with different impurity of Fe, Metals 11 (2021) 174.

[28] A. Wagiman, M.S. Mustapa, R. Asmawi, S. Shamsudin, M.A. Lajis, Y. Mutoh, A review on direct hot extrusion technique in recycling of aluminium chips, Int. J. Adv. Manuf. Technol. 106 (2020) 641–653.

[29] K. Al-Helal, J.B. Patel, Z. Fan, Fe-rich intermetallic formation and mechanical properties of recycled AA6111 alloy strips produced by melt conditioning twin roll casting, JOM 72 (2020) 3753–3759.

[30] Y.L. Zhao, D.F. Song, H.L. Wang, Y.W. Jia, B. Lin, Y. Tang, Y. Tang, D. Shu, Z.Z. Sun, Y.N. Fu, W.W. Zhang, Revealing the influence of Fe on Fe-rich phases formation and mechanical properties of cast Al-Mg-Mn-Fe alloys, J. Alloy. Compd. 901 (2022), 163666.

[31] X. Zhu, P. Blake, K. Dou, S. Ji, Strengthening die-cast Al-Mg and Al-Mg-Mn alloys with Fe as a beneficial element, Mater. Sci. Eng. A 732 (2018) 240–250.

[32] B. Lin, H. Li, R. Xu, Y. Zhao, H. Xiao, Z. Tang, S. Li, Thermal exposure of Al-Si-Cu-Mn-Fe alloys and its contribution to high temperature mechanical properties, J. Mater. Res. Technol. 9 (2020) 1856–1865.

[33] B. Lin, W. Zhang, X. Zheng, Y. Zhao, Z. Lou, W. Zhang, Developing high performance mechanical properties at elevated temperature in squeeze cast Al-Cu-Mn-Fe-Ni alloys, Mater. Charact. 150 (2019) 128–137.

[34] Z. Fan, F. Gao, Y. Wang, H. Men, L. Zhou, Effect of solutes on grain refinement, Prog. Mater. Sci. 123 (2022), 100809.

[35] Z.P. Que, Y. Wang, Y.P. Zhou, L. Liu, Z. Fan, Effect of Al-5Ti-1B grain refiner addition on the formation of intermetallic compounds in Al-Mg-Si-Mn-Fe alloys, Mater. Sci. Forum 828–829 (2015) 53–57.

[36] M.H. Khan, A. Das, Z. Li, H.R. Kotadia, Effects of Fe, Mn, chemical grain refinement and cooling rate on the evolution of Fe intermetallics in a model 6082 Al-alloy, Intermetallics 132 (2021), 107132.

[37] J.M. Yu, T. Hashimoto, H.T. Li, N. Wanderka, Z. Zhang, C. Cai, X.L. Zhong, J. Qin, Q.P. Dong, H. Nagaumi, X.N. Wang, Formation of intermetallic phases in unrefined and refined AA6082 Al alloys investigated by using SEM-based ultramicrotomy, J. Mater. Sci. Technol. 120 (2022) 118–128.

[38] S. Kumar, K.A.Q. O'Reilly, Influence of Al grain structure on Fe bearing intermetallics during DC casting of an Al-Mg-Si alloy, Mater. Charact. 120 (2016) 311–322.

[39] J. Rakhmonov, G. Timelli, F. Bonollo, Influence of melt superheat, Sr modifier, and Al-5Ti-1B grain refiner on microstructural evolution of secondary Al-Si-Cu alloys, Metall. Mater. Trans. A 47 (2016) 5510–5521.

[40] A. Lui, P.S. Grant, I.C. Stone, K.A.Q. O'Reilly, The role of grain refiner in the nucleation of AlFeSi intermetallic phases during solidification of a 6xxx aluminum alloy, Metall. Mater. Trans. A 50 (2019) 5242–5252.

[41] S.H. Rodríguez, R.E.G. Reyes, D.K. Dwivedi, O.A. González, V.H.B. Hernández, The effect of Al-5Ti-1B on microstructure and mechanical properties of Al-12Si-xFe alloy, Mater. Manuf. Process. 27 (2012) 599–604.

[42] S.K. Feng, E. Liotti, A. Lui, M.D. Wilson, T. Connolley, R.H. Mathiesen, P.S. Grant, In-situ X-ray radiography of primary Fe-rich intermetallic compound formation, Acta Mater. 196 (2020) 759–769.

[43] D.G. Eskin, J.W. Mi, Solidification Processing of Metallic Alloys Under External Fields, Springer, Materials Park, OH, 2018.

[44] G.I. Eskin, D.G. Eskin, Ultrasonic Treatment of Light Alloys Melts, second ed., CRC Press, Boca Raton, 2015.

[45] D.G. Eskin, I. Tzanakis, F. Wang, G.S.B. Lebon, T. Subroto, K. Pericleous, J. Mi, Fundamental studies of ultrasonic melt processing, Ultrason. Sonochem. 52 (2019) 455–467.

[46] F. Wang, D. Eskin, J. Mi, C. Wang, B. Koe, A. King, C. Reinhard, T. Connolley, A synchrotron X-radiography study of the fragmentation and refinement of primary intermetallic particles in an Al-35 Cu alloy induced by ultrasonic melt processing, Acta Mater. 141 (2017) 142–153.

[47] Z. Zhang, C. Wang, B. Koe, C.M. Schlepütz, S. Irvine, J. Mi, Synchrotron X-ray imaging and ultrafast tomography in situ study of the fragmentation and growth dynamics of dendritic microstructures in solidification under ultrasound, Acta Mater. 209 (2021), 116796.

[48] B. Wang, D. Tan, T.L. Lee, J.C. Khong, F. Wang, D. Eskin, T. Connolley, K. Fezzaa, J. Mi, Ultrafast synchrotron X-ray imaging studies of microstructure fragmentation in solidification under ultrasound, Acta Mater. 144 (2018) 505–515.

[49] Y. Zhao, W. Zhang, F. Meng, Z. Wang, D. Zhang, C. Yang, Microstructure and mechanical properties of as-cast Al-5.0Cu-0.6Mn-0.6Fe alloy produced by ultrasonic vibration and applied pressure, Rare Metal Mater. Eng. 47 (2018) 457–462.

[50] L. Zhang, X. Li, R. Li, R. Jiang, L. Zhang, Effects of high-intensity ultrasound on the microstructures and mechanical properties of ultra-large 2219 Al alloy ingot, Mater. Sci. Eng. A 763 (2019), 138154.

[51] J. Li, F. Li, S. Wu, S. Lü, W. Guo, X. Yang, Variation of microstructure and mechanical properties of hybrid particulates reinforced Al-alloy matrix composites with ultrasonic treatment, J. Alloy. Compd. 789 (2019) 630–638.

[52] Y. Yang, Z. Liu, R. Jiang, R. Li, X. Li, Microstructural evolution and mechanical properties of the AA2219/TiC nanocomposite manufactured by ultrasonic solidification, J. Alloy. Compd. 811 (2019), 151991.

[53] Y. Jia, D. Song, N. Zhou, K. Zheng, Y. Fu, D. Shu, The growth restriction effect of TiCN nanoparticles on Al-Cu-Zr alloys via ultrasonic treatment, Ultrason. Sonochem. 80 (2021), 105829.

[54] H. Huang, L. Qin, H. Tang, D. Shu, W. Yan, B. Sun, J. Mi, Ultrasound cavitation induced nucleation in metal solidification: an analytical model and validation by real-time experiments, Ultrason. Sonochem. 80 (2021), 105832.

[55] H.M. Vishwanatha, J. Eravelly, C.S. Kumar, S. Ghosh, Dispersion of ceramic nano-particles in the Al-Cu alloy matrix using twostep ultrasonic casting and resultant strengthening, Mater. Sci. Eng. A 708 (2017) 222–229.

[56] C.J. Todaro, M.A. Easton, D. Qiu, G. Wang, D.H. StJohn, M. Qian, The effect of ultrasonic melt treatment on macro-segregation and peritectic transformation in an Al-19Si-4Fe alloy, Metall. Mater. Trans. A 48 (2017) 5579–5590.

[57] C.J. Todaro, M.A. Easton, D. Qiu, G. Wang, D.H. StJohn, M. Qian, Effect of ultrasonic melt treatment on intermetallic phase formation in a manganese-modified Al-17Si-2Fe alloy, J. Mater. Process. Technol. 271 (2019) 346–356.

[58] H.R. Kotadia, M. Qian, A. Das, Microstructural modification of recycled aluminium alloys by high intensity ultrasonication: Observations from custom, Al-2Si-2Mg-1.2Fe-(0.5,1.0)Mn alloys, J. Alloy. Compd. 823 (2020), 153833.

[59] Y. Xuan, T. Liu, L. Nastac, L. Brewer, I. Levin, V. Arvikar, The influence of ultrasonic cavitation on the formation of Fe-rich intermetallics in A383 alloy, Metall. Mater. Trans. A 49 (2018) 3346–3357.

[60] S. Chankitmunkong, D.G. Eskin, C. Limmaneevichitr, Structure refinement, mechanical properties and feasibility of deformation of hypereutectic Al–Fe–Zr and Al-Ni-Zr alloys subjected to ultrasonic melt processing, Mater. Sci. Eng. A 788 (2020), 139567.

[61] J. Barbosa, H. Puga, J. Oliverira, S. Ribeiro, M. Prokic, Physical modification of intermetallic phases in Al-Si-Cu alloys, Mater. Chem. Phys. 148 (2014) 1163–1170.

[62] C. Lin, S.S. Wu, S.L. Lü, P. An, L. Wan, Effects of ultrasonic vibration and manganese on microstructure and mechanical properties of hypereutectic Al-Si alloys with 2% Fe, Intermetallics 32 (2013) 176–183.

[63] Y.B. Zhang, S. Kateryna, T.J. Li, Effect of ultrasonic treatment on formation of iron-containing intermetallic compounds in Al-Si alloys, China Foundry 13 (2016) 316–321.

[64] G. Wang, M.S. Dargusch, D.G. Eskin, D.H. StJohn, Identifying the stages during ultrasonic processing that reduce the grain size of aluminum with added Al3Ti1B master alloy, Adv. Eng. Mater. 19 (2017) 1700264.

[65] H.R. Kotadia, M. Qian, D.G. Eskin, A. Das, On themicrostructural refinement in commercial purity Al and Al-10wt% Cu alloy under ultrasonication during solidification, Mater. Des. 132 (2017) 266–274.

[66] Z. Liu, Z. Dong, X. Cheng, Q. Zheng, J. Zhao, Q. Han, On the supplementation of magnesium and usage of ultrasound stirring for fabricating in situ TiB$_2$/A356 composites with improved mechanical properties, Metall. Mater. Trans. A 49 (2018) 5585–5598.

[67] J. Zhao, X. Wu, L. Ning, J. Zhang, C. Han, Y. Li, Wetting of aluminium and carbon interface during preparation of Al-Ti-C grain refiner under ultrasonic field, Ultrason. Sonochem. 76 (2021), 105633.

[68] M. Easton, D. StJohn, Grain refinement of aluminum alloys: part I. the nucleant and solute paradigms—a review of the literature, Metall. Mater. Trans. A 30 (1999) 1613–1623.

[69] D.H. StJohn, P. Cao, M. Qian, M.A. Easton, A new analytical approach to reveal the mechanisms of grain refinement, Adv. Eng. Mater. 9 (2007) 739–746.